An Approach to Unsupervised Detection of Fully and Partially Destroyed Buildings in Multitemporal VHR SAR Images

Davide Pirrone ⓘ, *Member, IEEE*, Francesca Bovolo ⓘ, *Senior Member, IEEE*,
and Lorenzo Bruzzone ⓘ, *Fellow, IEEE*

Abstract—In the presence of abrupt change events, multitemporal synthetic aperture radar (SAR) data represent a precious supporting tool for quantifying changes, in particular in urban areas. A large amount of SAR data also exists at very high resolution (VHR). Over urban areas, the introduction of the VHR imagery moves the analysis down to the single building scale. However, VHR imagery is also characterized by a large heterogeneity and a more complex representation of the building. In this work, we propose a geometrical model for describing partially destroyed buildings and derive the corresponding multitemporal backscattering signature by applying the ray-tracing method. The model is integrated into an unsupervised automatic approach for the detection of both fully and partially destroyed buildings. The strategy considers a hierarchical structure of the changes. Experimental results conducted on two multitemporal VHR SAR datasets show a large robustness of the approach and good accuracy in the detection of the classes for damaged buildings with different severity levels.

Index Terms—Change detection (CD), damage assessment, fully destroyed buildings, fuzzy-based analysis, partially destroyed buildings, remote sensing, synthetic aperture radar (SAR), very high resolution (VHR).

I. INTRODUCTION

REMOTE sensing imagery from synthetic aperture radar (SAR) has proven a relevant role in multitemporal analysis for change detection (CD), with multiple applications. Some of them focus on long-time phenomena [1], [2] and use image time series; others focus on sharp changes [3]–[6] with a bitemporal analysis. These applications may assume an evident importance in the presence of urban areas and in case of abrupt events, such as natural hazards (e.g., flood [7] or earthquake [8]). SAR imagery maps scattering information and is affected by both geometrical distortions and speckle noise, which make the interpretation a complex task. However, SAR shows low sensitivity to both weather and sunlight conditions, which makes it suitable for multitemporal applications, as it guarantees acquisitions with a small temporal baseline, where some of the optical sensors may not perform well [9].

Let us consider SAR systems acquiring scattering information with no polarimetric content (i.e., a single polarimetric channel). Among them, SAR systems can be characterized in terms of the different geometrical resolution. Many sensors present a geometrical resolution in the order of decades of meters (i.e., medium resolution, MR). However, some SAR missions, such as the in-operation TerraSAR-X or the forthcoming Cosmo-SkyMed Second Generation, have been equipped with enhanced imaging capabilities, showing a resolution down to the meter scale (i.e., very high resolution, VHR). Therefore, if the MR SAR imagery leads the analysis to a city block scale, the VHR SAR imagery improves the analysis capabilities down to the building scale [10]–[12]. In the VHR SAR imagery, the metric-level spatial resolution and the off-nadir imaging geometry make that a low number of elementary scatterers be present in the resolution cell, corresponding to different elements of the building structure. This leads to a complex and heterogeneous scattering pattern for the building [13]. However, the fine resolution increases the heterogeneity in the image, as the reduced number of scatterers in the resolution cell makes the speckle noise not fully developed [9]. An alternative perspective to identify heterogeneous scattering contributions on urban targets is represented by polarimetric SAR imagery, which provides information on multiple polarimetric channels. Polarimetric target decompositions have been proposed in the literature in order to discriminate targets with different scattering behavior. In particular, this has been exploited in the detection of urban areas from single-time polarimetric images. Few works addressed the damage analysis of urban areas with multitemporal polarimetric data [14]–[16], mostly because of the possibility of obtaining multitemporal full-polarimetric data, especially with very high spatial resolution.

Instead, several works addressed the problem of CD in urban areas with single-polarimetric VHR SAR data. They include the supervised analysis of backscattering patterns in the postevent SAR image [17], [18], the joint analysis of VHR SAR and optical

Davide Pirrone is with the Center for Information and Communication Technology, Fondazione Bruno Kessler, I-38123 Trento, Italy, and also with the Department of Information Engineering and Computer Science, University of Trento, I-38123 Trento, Italy (e-mail: davide.pirrone.fbk@gmail.com).

Francesca Bovolo is with the Center for Information and Communication Technology, Fondazione Bruno Kessler, I-38123 Trento, Italy (e-mail: bovolo@fbk.eu).

Lorenzo Bruzzone is with the Department of Information Engineering and Computer Science, University of Trento, I-38123 Trento, Italy (e-mail: lorenzo.bruzzone@ing.unitn.it).

data [12], [19], [20], the use of ancillary information coming from GIS layers with SAR data [5], [21], and the multitemporal analysis of VHR SAR data in an unsupervised manner [6], [7], [22]–[27].

When considering meter-scale resolution, the data complexity makes the pixel- and region-based approaches for MR data not completely reliable for the CD analysis, thus analyses based on a higher semantic level were conducted in [22] and [28]. These analyses require the definition of a backscattering model of the object for associating a label of changed buildings to changes in the scattering properties. Several models have been presented in the literature. Some of the building models aim at preserving the radiometric information, by means of an accurate scattering model taking into account geometric and dielectric parameters of the target [29]. Others are devoted to the preservation of the geometrical accuracy, by using the ray-tracing method, which models the scattering and the propagation through optical rays [30]–[32].

A large interest in the literature has been devoted to the detection of changes with size comparable to the one typical of the building [22]. These are namely the changes from no building to a complete standing building and vice versa. These changes are named building construction and building full destruction, respectively. A different situation considers buildings for which only a part of the structure is affected by the damage. The effect of the damage on the building pattern should be larger than the VHR SAR resolution, in order to be detectable. We refer to this event as *building partial destruction*. In spite of the effort for the detection of building construction and full destruction, no effort has been spent in tackling with automatic approaches in the partial destruction case. The latter was mainly conducted by considering visual inspection of the operator who interprets the image features thanks to the *a priori* knowledge of the SAR imaging geometry and possibly considering the output of detailed SAR image simulators [11], [33]–[35]. Nevertheless, partially destroyed buildings have the same relevance as the fully destroyed ones and together may provide enhanced information for rescue and emergency services.

In this article, we aim at proposing a model for the multitemporal backscattering analysis of buildings partial destruction. The model assumes that the damage impacts the satellite-facing part and is based on geometrical assumptions about the shape of both the building and the damage. A backscattering analysis based on the ray-tracing method in single time is conducted on the target (i.e., the partially destroyed building) by varying the size parameters of the structure and/or the angles with respect to the SAR sensing direction. The model is highly complex because of the way the damage perturbs the geometry of the building. The multitemporal backscattering signature of the change is hence derived by comparison of the undamaged and damaged building models. A sensitivity analysis is conducted by varying the geometrical parameters and common elements of the multitemporal backscattering patterns are inferred and evaluated, to establish the multitemporal behavior of the partial damage.

The novel model for the building partial destruction is integrated in an automatic unsupervised CD strategy [22] designed originally for the detection of fully destroyed buildings only. The resulting approach exploits a hierarchical rationale, based on the different expected size of the changes, for identifying both building full and partial destructions. The kind of building damage is individuated from the backscattering variation by considering the possible candidates and the expected change size. For each candidate, spatial properties of the pattern are evaluated based on the proposed multitemporal scattering model. These properties are evaluated through fuzzy membership functions in order to measure the goodness of the building candidate.

The rest of this article is structured as follows. Section II presents the single-time scattering behavior for the building for different conditions (i.e., standing and fully and partially destroyed). In Section III, the multitemporal scattering behavior associated with both building full and partial destructions is derived by comparing the single-time models. In Section IV, the proposed automatic strategy for the detection of the different damage severity from multitemporal VHR SAR data is described. In Section V, experimental results are illustrated. Finally, in Section VI, conclusions and final remarks for future developments are traced.

II. BUILDING SCATTERING MODEL IN SINGLE-TIME VHR SAR IMAGES

In this section, a single-time scattering model is presented for the building under different damage conditions. We recall models for both standing and fully destroyed buildings from the literature [22], [31]. Based on the same paradigm, a novel geometrical model for a partially destroyed building is proposed and the corresponding scattering pattern is derived. In general, in the perspective of scattering unsupervised change detection, the multitemporal information from complex urban objects need to be rendered into a set of patterns being robust to the target structure variability. Thus, some simplifying geometrical assumptions on the target shape need to be made. The scattering is then derived with a ray-tracing technique based on them. Let us consider a flat-roof building with rectangular shape. Let H and W and L be its height and planar dimensions, respectively. Let θ be the incidence angle of the sensor. For typical imaging radar missions, θ is a value in the $[20°, 55°]$ interval. The building is considered as generally rotated with respect to the range-azimuth plane, with orientation angle ϕ defined between the segment W and the ground-range direction. ϕ ranges in the interval $[-\pi, \pi]$.

The scattering model is based on some simplifying assumptions about the problem geometry and the application of the ray-tracing method. The first assumption considers no perturbations from external elements on the building scattering signature (i.e., isolated building). This is true if the density of buildings is not higher than what is required to discriminate the backscattering contributions of a building at the resolution of the considered SAR images. The second assumption considers a structure with fixed height along one or both planar dimensions. With these assumptions, the ray-tracing method considers building slices
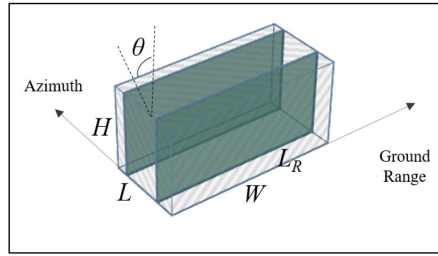
(a)
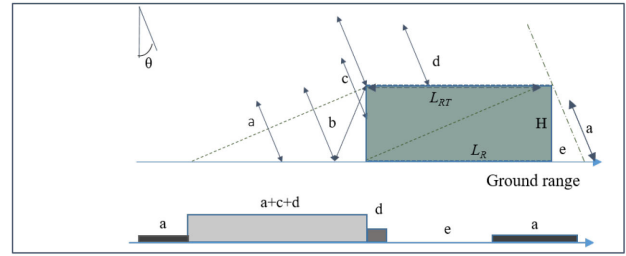
(b)

Fig. 1. Standing building. (a) Acquisition geometry and building slices for $\phi = 0$. (b) Backscattering profile for a single slice (only surface scattering), $L_R \geq L_{RT}$. Scattering terms: a (ground), b (double bounce), c (wall), d (roof), and e (shadow). The signature is represented in ground range.

TABLE I
HOMOGENEOUS SURFACE-SCATTERING REGIONS FOR STANDING BUILDING SCENARIO

Case	Geometrical condition	Surface scattering contributions (near- to far-range)
1	$L_R \geq L_{RT}$	$a + c + d; d; e$
2	$L_R < L_{RT}$	$a + c + d; a + c; e$

along ground range and scattering propagation with linear trajectories. The scattering terms are grouped into surface scattering and additive multibounce contributions, associated with either the surface targets or the corner reflectors, respectively. The building scattering analysis is conducted by first assuming the case of $\phi = 0$. The assumption is later removed and the analysis for the general case $\phi \neq 0$ is conducted. Each scattering analysis focuses on the surface scattering and additive multiple bounce contributions separately.

A. Standing Building

Let us assume that the building is aligned to the range direction (i.e., $\phi = 0$). In the analysis of the backscattering signature, we apply the ray-tracing method and consider building slices (green rectangles in Fig. 1(a) along the range direction. Each slice is characterized by a width L_R and a height profile h assuming value H on the building and 0 outside. For $\phi = 0$, L_R coincides with the planar dimension W (i.e., $L_R = W$) and all the slices show the same behavior.

Surface scattering: The contributions for the backscattering coefficient are considered from different building elements, namely the ground (a), the vertical wall (c), and the roof (d). The SAR system senses the target with incidence angle θ and this introduces layover and shadow effects for the contributions, with terms $a + c + d$ and e, respectively. Fig. 1(b) gives an example of the backscattering signature for the single building slice. Two signatures for the surface scattering are possible, depending on the value of L_R compared to a threshold L_{RT} [12], [22], [31]. L_{RT} is defined in terms of the building height (H) and the incidence angle (θ) as follows:

$$L_{RT} = H \cot \theta. \tag{1}$$

For $L_R \geq L_{RT}$, the layover and the shadow regions are separated by a region of scattering from the roof d. For $L_R < L_{RT}$, a second layover region exists, with contribution $a + c$. Table I
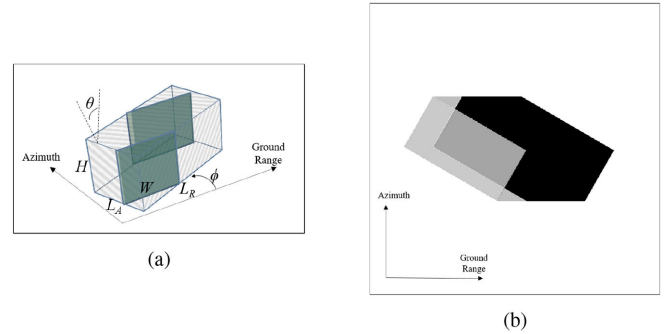

(a)

(b)

Fig. 2. Standing building with $\phi = -\pi/6$. (a) Acquisition geometry and building slices. (b) Example of a backscattering pattern for a standing building, with $W > H \cot \theta$ and $\phi = \pi/4$ ($K_a = 0.2$, $K_c = K_d = 5$).

indicates the sequence of surface scattering regions seen from near to far range for the two cases.

Multibounce contributions: A double-bounce contribution b_{wg} for the backscattering coefficient is created by the corner reflector formed by the standing wall (w) and the ground (g). This contribution is reflected to the sensor with an angle θ [36].

In order to model the angular dependence of the backscattering coefficient for the different pattern regions, terms a, c, and d are modeled by assuming the Lambert law for the radiation as follows:

$$s = K_s \cos^2 \hat{\theta}, s \in \{a, c, d\} \tag{2}$$

where $\hat{\theta}$ is the angle between the surface normal and the scattering direction (i.e., $\hat{\theta} = \theta$ for a, d and $\hat{\theta} = \pi/2 - \theta$ for c terms, respectively). For the double-bounce contribution b_{wg}, a dihedral model with equal plates has been considered [37]. Based on these considerations, a simple model for b_{wg} has been considered

$$b_{wg} \sim H \sin^2(\theta + \pi/4) \approx H \sin \theta \cos \theta. \tag{3}$$

Let us now remove the assumption of $\phi = 0$ and consider a generic value of ϕ. In this case, each slice has width L_R and a height profile with value H on the building. L_R depends on the azimuth position, the building size, and the building orientation. Fig. 2(a) illustrates the acquisition geometry and the slices (green rectangles) for an oriented building. Slices with $L_R \geq L_{RT}$ present a backscattering signature as described in Case 1 of Table I. Conversely, those with $L_R < L_{RT}$ present
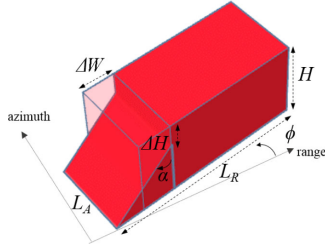
Fig. 3.   Geometric model for the partially destroyed building.

a backscattering signature as described in Case 2 of Table I. Additive double-bounce contribution b_{wg} is introduced in the scattering signature by the corner reflector on each slice [22]. By considering all the slices and superimposing surface scattering and multiple-bounce contributions, a 2-D backscattering pattern is derived for the standing building. Fig. 2(b) shows an example of the 2-D backscattering pattern for $\phi = \pi/4$.

B. Fully Destroyed Building

For every orientation angle, the fully destroyed building presents a backscattering signature with surface scattering contributions from the ground (a) and the uncovered bare soil (f), with similar values. No multiple-bounce contributions exist. Thus, the backscattering signature can be considered as almost constant over range and azimuth [22].

C. Novel Model for Partially Destroyed Building

In this section, we illustrate the proposed model for a partially destroyed building. Let us assume the same building described in Section II-A. Let us assume that a portion of the satellite facing facade in near range falls down [34]. Since the facades in far range are occluded because the SAR geometry damages located in the far range need images acquired in complementary acquisition direction, where they appear in near range and the model applies the same as illustrated next. Fig. 3 illustrates the geometric model for the partially destroyed building. For the sake of simplicity, the geometrical model is assumed to have constant height along the direction determined by L.

The fallen part of the building is defined by height H, slope α, and planar dimensions ΔW and L. The fall produced a debris with surface slope α with respect to the nadir and planar dimensions $(H - \Delta H) \tan \alpha$ and L, respectively. Moving to far range, the debris is followed by the undamaged part of the building, with height H and range and azimuth dimensions $W - \Delta W$ and L, respectively. Under the simplifying assumption that volume is preserved while the building is falling down, the three parameters $\{\alpha, \Delta H, \Delta W\}$ satisfy the following equation:

$$\Delta W = \frac{(H - \Delta H)^2}{2H} \tan \alpha. \qquad (4)$$

Each slice of the building is characterized by a total width L_R and a height profile h. For $\phi = 0$, all the slices have size $L_R = W - \Delta W + (H - \Delta H) \tan \alpha$. h keeps the same height value for all the slices [see profiles in the green rectangles of

TABLE II
SURFACE SCATTERING CONTRIBUTIONS FOR A PARTIALLY DESTROYED BUILDING

Case	Geometrical condition	Surface scattering contributions (near- to far-range)
1	$L_R \geq L_{RT2}$	$a; a + c_w + d; a + c_d + d; d; e$
2	$L_{RT1} \leq L_R < L_{RT2}$	$a; a + c_w + d; a + c_d + d; a + c_d; e$
3	$L_R < L_{RT1}$	$a; a + c_w + d; a + c_w; a + c_d; e$

Fig. 4(a)], namely a ramp rising from 0 to $H - \Delta H$, with constant slope $\pi/2 - \alpha$, on the damaged part and a constant value H on the nondamaged part, respectively. Each slice shows the same scattering behavior.

Surface scattering: Because of the off-nadir acquisition angle θ, the missing layover from the fallen part shifts the signature to far range. The contributions to the backscattering coefficient are considered from both building and debris elements, namely ground (a), the vertical part of the wall (c_w), the debris surface (c_d), and the roof (d). Fig. 4(b) illustrates an example of the surface scattering for the single slice of a partially destroyed building for $\phi = 0$. The slice signature is characterized by the presence of layover and shadow effects, with regions $a + c_w + d$ and e, respectively. The two regions are separated by two scattering regions depending on the value of L_R compared to thresholds L_{RT1} and L_{RT2}. L_{RT1} and L_{RT2} are defined in terms of the incidence angle θ and building parameters α and ΔH as follows:

$$L_{RT1} = H \cot \theta \qquad (5)$$

$$L_{RT2} = \Delta H \cot \theta + (H - \Delta H) \tan \alpha. \qquad (6)$$

For $L_R \geq L_{RT2}$, the two regions are separated by a layover region $a + c_d + d$ and a region of scattering from the roof d. On the other hand, if $L < L_{RT1}$, the two regions are separated by two layover regions with values $a + c_w$ and $a + c_d$, respectively. Intermediate cases (i.e., $L_{RT1} \leq L_R < L_{RT2}$) show two layover regions with values $a + c_d + d$ and $a + c_d$. The geometrical conditions and the corresponding backscattering regions for a single slice are summarized in Table II.

Multibounce contributions: The presence of the debris surface both reduces the double-bounce region associated with the corner reflector and introduces two possible multibounce contributions for the backscattering coefficient, derived according to geometrical considerations [36]. These contributions may either exist or not depend on the parameters θ, α, H, and ΔH. The first one is the double bounce b_{dg} [green color in Fig. 4(c)] related to the interaction of the debris (d) and the ground (g), which is reflected to the sensor with an angle $2\alpha + \theta$. The second contribution is the triple bounce b_{wdg} [orange color in Fig. 4(c)] related to the interaction among the vertical part of the wall, the debris, and the ground, which is reflected to the sensor with an angle $2\alpha - \theta$. Both angles are assumed existing in the interval $(0; \pi/2)$. The effect of the orientation angle ϕ on all the multiple-bounce contributions is assumed to be negligible. The possible cases are summarized in Table III.

Terms a, c_d, c_w, and d are modeled by assuming the Lambert law for the radiation

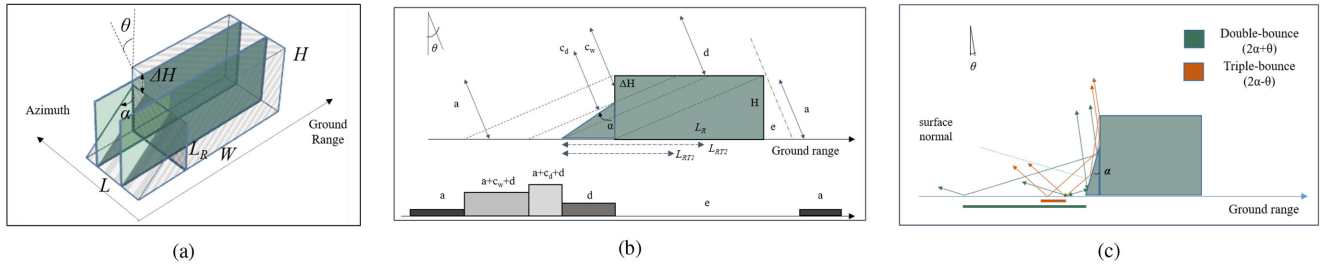$$s = K_s \cos^2(\hat{\theta}), \ s \in \{a, c_d, c_w, d\} \qquad (7)$$

Fig. 4.   Partially destroyed building. (a) Acquisition geometry and building slices for $\phi = 0$. (b) Backscattering signature with surface scattering contributions for a single slice based on the ray-tracing method, $L_R \geq L_{RT2}$. Scattering terms: a (ground), c_w (wall), c_d (debris), d (roof), and e (shadow). (c) Multiple bounce contributions introduced by the debris (single slice). The slice is sensed with an incidence angle θ.

TABLE III
MULTIBOUNCE CONTRIBUTIONS FOR A PARTIALLY DESTROYED BUILDING

Case	Geometrical condition	Multi-bounce contributions (near- to far-range)
1	$\theta \geq \alpha$	Double bounce from vertical wall (θ); Double bounce from debris ($2\alpha + \theta$);
2	$\theta < \alpha$ $H \tan \theta \geq (H - \Delta H) \tan \alpha$	Double bounce from vertical wall (θ) Double bounce from debris ($2\alpha + \theta$); Triple bounce ($2\alpha - \theta$).
3	$\theta < \alpha$ $H \tan \theta < (H - \Delta H) \tan \alpha$	Double bounce from debris ($2\alpha + \theta$); Triple bounce ($2\alpha - \theta$).

where $\hat{\theta}$ is the angle between the surface normal and the incidence direction (i.e., $\hat{\theta} = \theta$ for a, d, $\hat{\theta} = \pi/2 - \theta$ for c_w, and $\hat{\theta} = \pi/2 - \theta - \alpha$ for c_d). Because of the similar material, debris and the wall are assumed to have similar dielectric properties and coefficients K_{c_d} and K_{c_w} (i.e., $K_{c_d} \simeq K_{c_w} = K_c$). For the backscattering associated with the multiple-bounce contributions, we rely on the same considerations expressed for b_{wg}. The models for both b_{dg} and b_{wdg} are expressed as follows:

$$b_{dg} \sim K_a K_c \cos(2\alpha + \theta) \sin(\alpha + \theta) \qquad (8)$$

$$b_{wdg} \sim \cos(2\alpha - \theta) \sin(\alpha - \theta). \qquad (9)$$

By considering all the slices and superimposing surface scattering and multiple-bounce contributions, a 2-D scattering pattern is derived for the partially destroyed building.

Let us now consider a generic angle $\phi \neq 0$. To constrain the damage to the satellite-facing facade, ϕ is limited to the interval $[-\pi/2, \pi/2]$. Other values refer to a building with damages on one of the occluded facades. Without loss of generality, we focus the analysis for positive ϕ values. The patterns for the corresponding negative values can be derived by applying the same procedure. The building slices are now characterized by width L_R and height profile h, depending on the azimuth position, the geometrical parameters, and the orientation angle. Furthermore, the slices of the oriented building present debris with a slope angle β with respect to the vertical direction. β depends on both angles α and ϕ as follows:

$$\beta = \arctan(\cot \alpha \cos \phi). \qquad (10)$$

Four kinds of height profile can be associated with h for the general case, namely profiles A, B, C, and D. Each of the height profiles can be described together with its backscattering analysis, derived by applying the ray-tracing as follows.

1) *Profile A* (yellow in Fig. 5): The slice only includes the debris. h assumes values rising from 0 to $L_R \cot \beta$ with constant slope $\pi/2 - \beta$. The corresponding backscattering signature is composed by contributions a and c_d. Layover of the two contributions occurs for $\beta < \pi/2 - \theta$ values. Double-bounce term b_{dg} may occur depending on the conditions described in Table III.

2) *Profile B* (dark green in Fig. 5): Depending on the value of ϕ, the profile has two possible behaviors. For small values of ϕ (i.e., $\phi \leq \phi_0$), the slice includes both the debris and the undamaged part. h assumes values rising from 0 to $H - \Delta H$ with constant slope $\pi/2 - \beta$ associated with the near-range debris and constant value H on the far-range undamaged part of the building. In this case, the backscattering signature is characterized by surface scattering and multiple bounce contributions as described in the analysis for $\phi = 0$ (see Tables II and III), with angle β for the slice.

Conversely, for large values of ϕ (i.e., $\phi > \phi_0$), the slice only includes the debris and height profile assumes values rising from value h_0 to $h_0 + L_R \cot \beta$ with constant slope $\pi/2 - \beta$, where $h_0 \in [0, H - \Delta H - L_R \cot \beta]$. The corresponding backscattering signature is similar to that in Table I, with a region of layover $a + c_d + c_w$ and a region of shadow e. Two possible multibounce contributions, with angles θ and $2\alpha + \theta$, are associated with the corner reflector of h_0 and the debris slope, respectively. ϕ_0 is derived based on geometrical considerations as follows:

$$\phi_0 = \arcsin \left[\frac{L_A \cos \phi}{(H - \Delta H) \tan \alpha \sin \phi} \right]. \qquad (11)$$

3) *Profile C* (brown in Fig. 5): The slice includes both the debris and the undamaged part. The height profile assumes values rising from h_1 to $H - \Delta H$ with constant slope $\pi/2 - \beta$ associated with the near-range debris and a constant value H on the far-range undamaged part of the building, $h_1 \in [H - \Delta H - L_R \cot \beta; H - \Delta H]$. For the corresponding backscattering signature, same considerations traced above for $\phi = 0$ hold. Two further contributions are associated with the positive value h_1, namely a decrease in the size along range of the regions associated with the c_w contribution and a double bounce region associated with the part of the debris with height h_1.
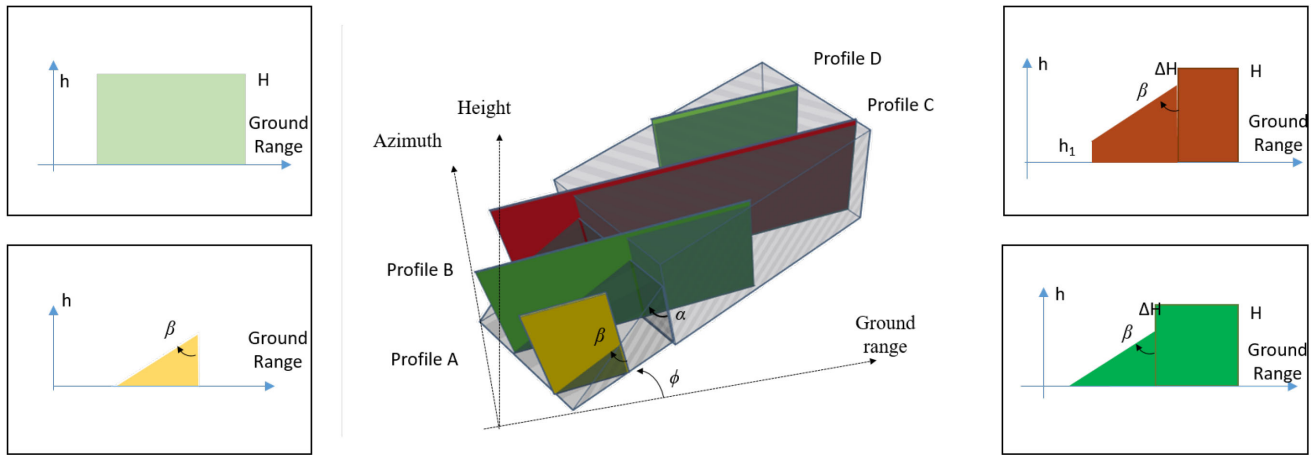
Fig. 5. Example of acquisition geometry of a partially destroyed building for $\phi \neq 0$ and building slices. Aspect angle effect generates four profiles, namely A (yellow), B (dark green), C (brown), and D (light green).
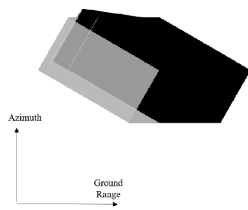

Fig. 6. Example of backscattering pattern for a partially destroyed building for $\phi = -\pi/6, \Delta H = H/4$, and $\alpha = \pi/6$ ($K_a = 0.2, K_c = K_d = 5$).

Fig. 7. (a) Multitemporal pattern for building full destruction, for $\phi = \pi/4$. Backscattering increase and decrease are represented in green and magenta, respectively. (b) Representation of the geometrical features associated with the pair of regions R_I (in green) and R_D (in magenta) for the multitemporal scattering pattern.

4) *Profile D* (light green in Fig. 5): The slice includes only the undamaged part. The backscattering signature is derived based on the considerations for the standing building slices in Section II-A.

By considering all the slices and superimposing surface scattering and multiple-bounce contributions, a 2-D backscattering pattern is derived for the partially destroyed building. Fig. 6 shows an example of a 2-D backscattering pattern for $\phi = \pi/4$, with damage parameters $\alpha = \pi/6, \Delta H = H/4$.

III. BUILDING SCATTERING MODEL IN MULTITEMPORAL VHR SAR IMAGES

Based on the single-time scattering models derived in Section II, a multitemporal analysis for the building damage assessment is conducted by comparing the patterns in pre-event and postevent. The expected behavior for the multitemporal pattern can be characterized by defining peculiar geometrical features on the change regions of the multitemporal scattering pattern. Two possible damage situations are considered. The first situation considers the complete destruction of building, by comparing patterns for standing and fully destroyed buildings associated with pre-event and postevent, respectively [22]. The second situation is a novel contribution of this work and considers the partial destruction of the building. This is obtained by considering the pattern of the standing building and the one of a partially destroyed building for the pre-event and postevent, respectively. The multitemporal comparison highlights presence of areas with
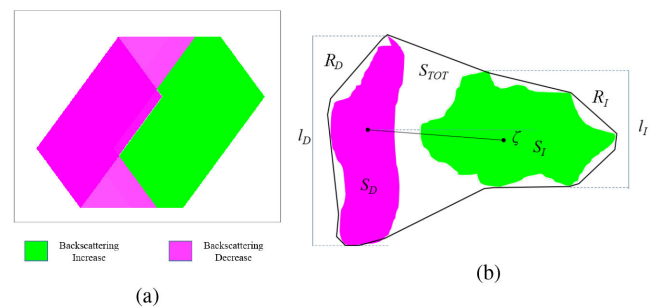
scattering increase (ω_I), decrease (ω_D), or no change (ω_{nc}) of scattering being peculiar for the two cases.

A. Building Full Destruction

For building full destruction, the multitemporal comparison generates a pattern with a large increase region R_I and multiple adjacent decrease regions [see Fig. 7(a)]. The increase region is associated with the disappearance of the building shadow in far range. The decrease regions are associated with the disappearance of the different scattering contributions associated with the building structure in near range. The opposite situation, describing the building construction, can be described in the multitemporal analysis of an increase region in near range and decrease region in the far range, respectively. For sake of simplicity in the multitemporal analysis, adjacent decrease regions are grouped into a single region R_D. R_D is characterized by area S_D and length l_D along the azimuth direction. Corresponding values S_I and l_I are defined for the increase region R_I. An area measure S_{TOT} is then defined for the convex hull of the two regions. Based on these spatial parameters, the following four spatial features can be defined for the pair of regions R_I and R_D,

in order to describe the multitemporal pattern for the building full destruction [see Fig. 7(b)].

1) Area ratio r_a : minimum ratio between the areas S_I and S_D

$$r_a = \min\left\{\frac{S_I}{S_D}, \frac{S_D}{S_I}\right\}. \qquad (12)$$

2) Azimuth length ratio r_l : minimum ratio between the lengths l_I and l_D

$$r_l = \min\left\{\frac{l_I}{l_D}, \frac{l_D}{l_I}\right\}. \qquad (13)$$

3) Orientation ζ : clockwise angle between the range direction and the line connecting the centroids of the two regions.

4) Total change ratio r_t : ratio between the sum of the areas S_D and S_I and the convex hull area S_{TOT}

$$r_t = \frac{S_D + S_I}{S_{\text{TOT}}}. \qquad (14)$$

From the literature, we expect that the ratio values tend to one (i.e., $r_a, r_l, r_t \simeq 1$), whereas orientation tend to zero ($\zeta \simeq 0$) [22].

B. Novel Model for Building Partial Destruction

The proposed multitemporal pattern for building partial destruction presents a sequence of regions along the range direction being more complex than the one of building full destruction and a dependence on both the orientation angle ϕ and the damage parameters ΔH and α. A general characterization of the pattern is thus conducted with a sensitivity analysis, by considering $\theta > \pi/4$ and $L_R > H \cot\theta$. We assume that K_c and K_d are similar and much larger than K_a (i.e., $K_c \simeq K_d, K_a \ll K_d$). ΔH and α are the free parameters ranging in $[H/4, 3H/4]$ and $[\pi/12, \pi/3]$, respectively. Very large values for parameters ΔH and α are associated with geometries that are not likely to occur in real scenarios and thus excluded. The orientation angle varies in $[0, \pi/3]$. Higher values make the damaged facade tend to be oriented along the azimuth direction, thus the slices of the multitemporal pattern tend to become close to profile D, with constant height on the slice.

Fig. 8 shows multitemporal backscattering patterns of the building partial destruction, derived for two damage options and two different orientation angles. For the sake of simplicity in the analysis, both adjacent increase and decrease regions are grouped into a single one. From near (subscript 1) to far (subscript 2) range, the multitemporal pattern is composed by the sequence of decrease (subscript dec), increase (subscript inc), and no change (subscript nc) in backscattering: $R_{\text{dec1}}, R_{\text{nc}}, R_{\text{inc1}}, R_{\text{dec2}},$ and R_{inc2} characterizing the damaged part; and a large no-change region, associated with the part of the building not affected by the damage. This no-change region is placed in far range, with geometry dependent on the building orientation. Most of the change regions tend to be oriented according to ϕ (i.e., uniform along azimuth for $\phi = 0$). Conversely, R_{inc2} is elongated in the range direction, with size decreasing for ϕ tending to zero. Decrease regions R_{dec1} and R_{dec2} are
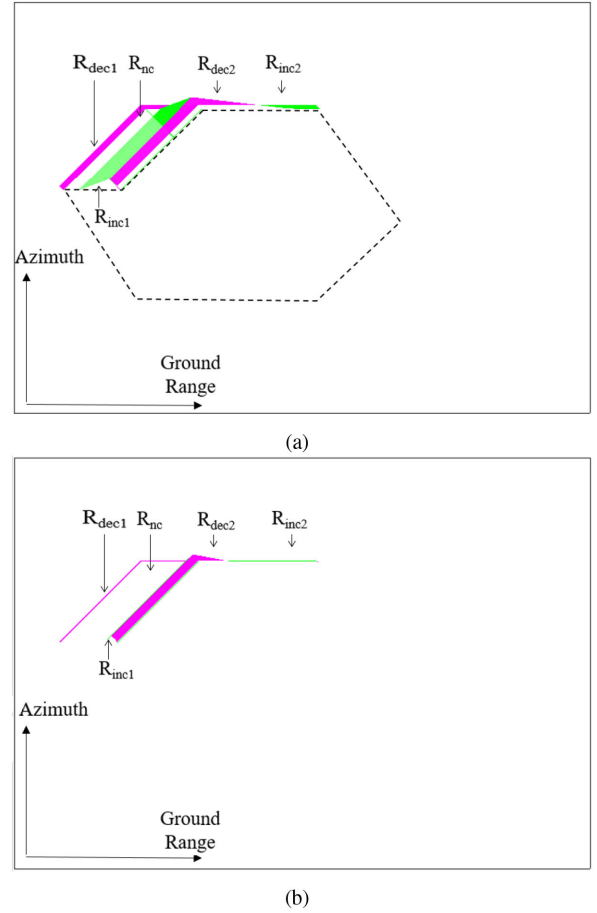

Fig. 8. LR Patterns for partially destroyed buildings with $\phi = -\pi/4$ and different values set for parameters $\{\alpha, \Delta H\}$. (a) $\{\pi/12, H/4\}$. (b) $\{\pi/6, 3H/4\}$. Areas of backscattering decrease and increase are represented in magenta and green, respectively.

associated with the fall of the debris both reducing the near-range layover region and widening the far-range region associated with d. No-change region R_{nc} is associated with the part of the facade footprint showing no variations in the total scattering. Increase region R_{inc1} is associated with the scattering from the debris $c_d > c_w$. Increase region R_{inc2}, located into slices corresponding to the profile A of Fig. 5, is caused by the far-range height, depending on angle β and is smaller than pre-event value H (i.e., $W \cot\beta < H$). This causes a reduction of the shadow in the multitemporal scattering.

For large values of ΔH, the width along ground range for all the decrease and increase regions tends to be small, whereas that for the no-change regions tends to be large. Large ΔH corresponds to small ΔW for (4), so that the damage tends to be limited and the slice tends to behave as the standing building one. Large α corresponds to large ΔW for (4). This widens the region with scattering d and makes R_{inc1} large. On the other hand, large α makes slices following profile A with a small height, and thus a small shadow region. In the multitemporal pattern, this makes R_{inc2} large along the range direction. Changes in the region sequence can be seen in the presence of a strong triple-bounce contribution in the backscattering pattern of the partially

destroyed building, generating a local increase of backscattering. Nevertheless, the presence of this term depends on both α and ϕ, as described earlier.

The multitemporal patterns in the sensitivity analysis are used for deriving a multitemporal backscattering prototype of the building partial destruction. In this work, patterns with similar characteristics have been considered by assuming the condition $\alpha < \pi/6$. A geometrical analysis of the regions has been conducted for this pattern, by focusing on two significant regions, namely the decrease region R_{dec1}, associated with the reduced size of the layover region, and the increase region R_{inc1}, associated with the layover with stronger scattering given by c_d. Change regions may be concave. Thus, the convex skull, defined as the largest convex polygon inscribed in the considered region [38], was selected for both R_{dec1} and R_{inc1}.

Let $\tilde{R}_I$ and $\tilde{R}_D$ be the convex skull approximation for R_{inc1} and R_{dec1}, respectively. Similarly to what defined in Section III-A, $\tilde{R}_I$ is characterized by area $\tilde{S}_I$ and length $\tilde{l}_I$, along the azimuth direction. Corresponding values $\tilde{S}_D$ and $\tilde{l}_D$ are defined for the region $\tilde{R}_D$. Let $\tilde{S}_{\text{TOT}}$ be the area of the convex hull of the pair $\tilde{R}_I$ and $\tilde{R}_D$. Based on these spatial parameters, the following four spatial features are defined for describing the multitemporal pattern for the building partial destruction.

1) Area fill ratio $\tilde{r}_a$: ratio between the areas $\tilde{S}_I$ and $\tilde{S}_D$

$$\tilde{r}_a = \frac{\tilde{S}_I}{\tilde{S}_D}. \tag{15}$$

2) Azimuth length ratio $\tilde{r}_l$: minimum ratio between the lengths $\tilde{l}_I$ and $\tilde{l}_D$

$$\tilde{r}_l = \min\left\{ \frac{\tilde{l}_I}{\tilde{l}_D}, \frac{\tilde{l}_D}{\tilde{l}_I} \right\}. \tag{16}$$

3) Orientation $\tilde{\zeta}$: clockwise angle between the range direction and the line connecting the centroids of $\tilde{R}_I$ and $\tilde{R}_D$.

4) Total change ratio $\tilde{r}_t$: ratio between the sum of the areas $\tilde{S}_I$ and $\tilde{S}_D$ and the convex hull area $\tilde{S}_{\text{TOT}}$

$$\tilde{r}_t = \frac{\tilde{S}_I + \tilde{S}_D}{\tilde{S}_{\text{TOT}}}. \tag{17}$$

IV. PROPOSED APPROACH FOR UNSUPERVISED BUILDING CD IN VHR SAR IMAGES

In this section, a novel automatic hierarchical strategy for the unsupervised detection of building changes with different semantic meaning is proposed. Let X_1 and X_2 be the two input intensity VHR SAR images, with size $M \times N$, acquired before and after the change event, respectively. The strategy aims at deriving a multiclass CD map with five classes $\{\omega_0, \omega_1, \omega_2, \omega_3, \omega_4\}$. The classes are described as follows:

1) area with no change (ω_0);
2) building full destruction (ω_1);
3) building construction (ω_2);
4) building partial destruction (ω_3); and
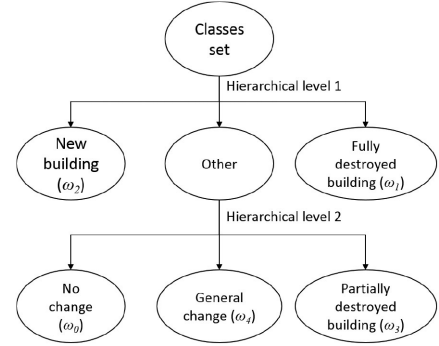5) change in backscattering not associated with buildings (ω_4).

Fig. 9.   Hierarchical representation of the building CD problem.

The novelty of the proposed strategy lies in both integrating the proposed scattering model for building partial destruction in an automatic building CD strategy and considering a change hierarchy associated with the different spatial scales (see Fig. 9) to formulate the CD problem. Classes are reported as $\{\omega_1, \omega_2\}$ for the first hierarchical level and $\{\omega_0, \omega_3, \omega_4\}$ for the second one. The decision on ω_0 is left to the second hierarchical level because the partially destroyed building model includes no-change information (see Section III-B). Fig. 10 illustrates the general block scheme of the proposed approach. The scheme namely presents: a processing stage for the multitemporal comparison and the generation of a backscattering CD map; fully destroyed building detection (FDBD) on the first hierarchical level, for identifying classes ω_1 and ω_2; a changed-building mask generation for removing ω_1 and ω_2 from the analysis at the second level; partially destroyed building detection (PDBD) on the second hierarchical level, for identifying classes ω_0, ω_3, and ω_4; and fusion of the building CD maps. Both FDBD and PDBD consider two steps. The first one is for detecting the best changed building candidates in the scattering CD map. The second one is associating a probability of representing a fully/partially destroyed or a new building to the candidates, based on the pattern geometrical parameters described in Sections III-A and III-B. The association is conducted via a set of fuzzy membership functions. The parameters used in the fuzzy set are tuned based on the model of the building and its robustness to noise and clutter.

A. Multitemporal Comparison and Backscattering CD

Multitemporal comparison of X_1 and X_2 is conducted by means of the log-ratio operator. The log-ratio image X_{LR} is defined as follows:

$$X_{\text{LR}} = \log \frac{X_2}{X_1}. \tag{18}$$

Log-ratio operator is frequently used as a pixel-based index in SAR CD analysis, as it both mitigates the speckle effect on the multitemporal information and highlights the increase and decrease of backscattering, which assumes positive and negative values in X_{LR}, respectively [22], [39]–[42]. Despite the large mitigation of the speckle effect, a residual noise contribution may still impact on the CD analysis. A multiscale decomposition
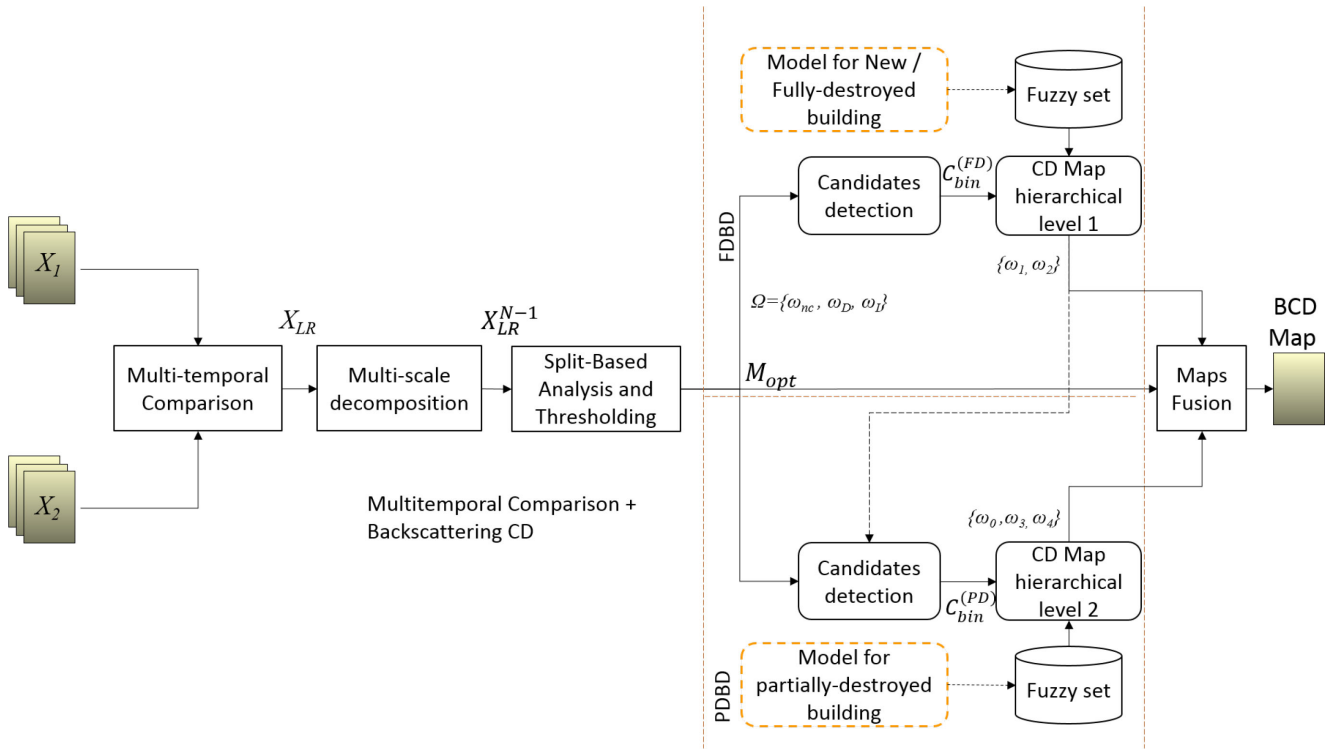
Fig. 10.   Block scheme of the proposed approach.

step is applied to X_{LR} in order to overcome these issues [22], [43]–[45]. The output of the decomposition process is a set of images $X_{\mathrm{LR}}^n, n = 0, ..., N - 1$. Images with large n have high robustness to noise but small level of detail and vice versa. In the wavelet decomposition, X_{LR} is assumed as X_{LR}^0 (i.e., $X_{\mathrm{LR}}^0 = X_{\mathrm{LR}}$). For this, 2-D discrete stationary wavelet transform (2D-SWT) is selected as a multiscale operator, following [22] and [44]. At scale level $N - 1$, changes on small elements are neglected, whereas the large ones are detected as homogeneous change areas. The optimal value N is chosen based on the minimum building footprint size, in order to preserve the edge information while mitigating the residual speckle effect.

Let $X_{\mathrm{LR}}^{\mathrm{opt}}$ be the decomposition at the optimal scale level (i.e., $X_{\mathrm{LR}}^{\mathrm{opt}} = X_{\mathrm{LR}}^{N-1}$). An unsupervised thresholding is performed on $X_{\mathrm{LR}}^{\mathrm{opt}}$, in order to derive a backscattering CD map with classes ω_I, ω_D, and ω_{nc}. The thresholding is performed according to the split-based analysis introduced in [3]. Let S_R and S_A be the dimensions of a split. Split-based analysis divides the image $X_{\mathrm{LR}}^{\mathrm{opt}}$ into splits with size $S_R \times S_A$ in order to have populations of ω_I and ω_D comparable to that of ω_{nc}. The variance of samples within the split is considered as a measure of change content (the higher the variance the higher the probability that changes exist in the split). A subset of splits with largest variance is defined for the threshold selection, based on a split selection parameter B. S_A and S_R are chosen based on the average building size on the scene, whereas B is tuned based on the application. Small B values correspond to a larger proportion of the total change information and vice versa.

A Bayesian thresholding is applied on the set of selected splits, by assuming that samples of the set be modeled as a mixture of three Gaussian distributions. Unknown prior probabilities and marginal distribution parameters are estimated with EM algorithm [42]. The estimated thresholds are then extended to the whole image and backscattering CD map M_{opt} is obtained.

B. Hierarchical Level 1: FDBD

Starting from M_{opt}, building CD is performed on each hierarchical level by detecting the changed-building candidates and then performing spatial analysis on each of them in order to detect classes. Changed-building candidates are generally associated with areas with a large density of changed pixels. The candidate detection is performed via a set of moving windows applied on the scattering CD map, following the approach in [22]. In order to capture most of the possible orientations for the changed-building candidates, five possible windows $W_\beta, \beta = 1, ..., 5$, with constant area and different geometry are considered in the analysis. The spatial analysis of the candidates is conducted by evaluating the geometry of the change regions (as defined in both Sections III-A and III-B) with a fuzzy inference system, in order to detect building classes.

For the first level, the changed building candidates are detected by using a sliding window with size parameters z_1 and z_2 on M_{opt}. Scanning from left to right, the total number of changed pixels inside the window is computed. Fig. 11 shows the set of the possible moving windows applied in the candidates detection. In particular, W_β includes four rectangular windows with size $z_1 \times z_2$ and different orientation angles (i.e., $\{\pi/2, \pi/4, 0, -\pi/4\}$) and a square window of size $\sqrt{z_1 z_2} \times \sqrt{z_1 z_2}$. As the FDBD is devoted to completely changed building candidates, the values
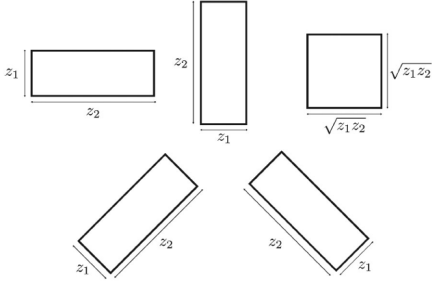
Fig. 11. Set of moving windows used for the candidate detection with dimensions z_1 and z_2.

(a)   (b)

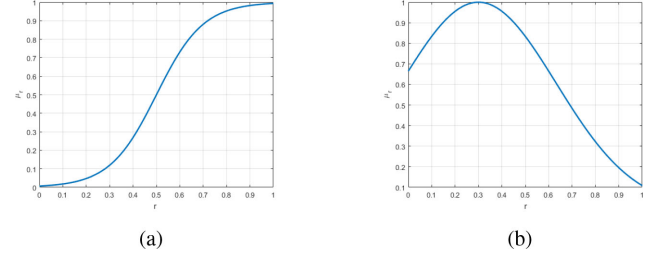Fig. 12. Examples of membership function. (a) Sigmoid function with $a = 10$ and $c = 0.5$. (b) Gaussian function with $\mu = 0.35$ and $\sigma^2 = 0.332$.

of z_1 and z_2 are selected based on the average building footprint size on the site.

Let $W_\beta(i,j), \beta = 1, ..., 5$, be one of the possible moving windows centered on the pixel (i,j), with size parameters $z_1 \times z_2$. Let $M_{W_\beta(i,j)}^{(\text{FD})} = M_{\text{opt}} | M_{\text{opt}} \subset W_\beta(i,j)$ be the set of pixels of M_{opt} in $W_\beta(i,j)$, indicating the amount of pixels belonging to ω_D or ω_I. A candidate index $C^{(\text{FD})}(i,j)$ for the pixel (i,j) can be defined as the maximum value of the set, indicating the amount of the change information detected in the set of windows

$$C^{(\text{FD})}(i,j) = \max_{\beta=1,...,5} \text{card}\left(M_{W_\beta(i,j)}^{(\text{FD})} \in \omega_D \wedge M_{W_\beta(i,j)}^{(\text{FD})} \in \omega_I \right) \tag{19}$$

where $\text{card}(\cdot)$ represents the cardinality of the set. Finally, a binary map of the candidates $C_{\text{bin}}^{(\text{FD})}$ is derived by thresholding $C^{(\text{FD})}$ with threshold value $T_C^{(\text{FD})}$. The set of candidates is extracted from $C_{\text{bin}}^{(\text{FD})}$ by considering the connected components of the changed regions and by applying the flood-fill algorithm with an eight-connected neighborhood [22], [46]. The threshold is chosen based on the size of the moving window (i.e., $T_C^{(\text{FD})} = \tau_{\text{FD}} z_1 z_2, 0 < \tau_{\text{FD}} \leq 1$).

A bounding box is traced for each of the candidates and all possible region pairs with an increase and a decrease region are considered for a spatial analysis. Without loss of generalization, let us assume that one region of decrease and one region of increase exist inside the single candidate box. If more regions of increase or decrease exist, spatial analysis is conducted on each possible pair and the one providing the best candidate score is assumed as most reliable. The spatial analysis of the region pair is conducted with a fuzzy inference system based on the geometrical parameters of the pair [47]. The analysis focus on the set r_l, r_a, r_t, ζ. As described in Section III-A, reliable values of r_a, r_t, and r_l are expected to be close to 1, as there is no sensible prevalence of the values of either R_I or R_D. On the other hand, reliable values of ζ are expected to be close to zero [22]. Thus, for the evaluation, sigmoid membership functions $\Sigma_l(r_l, a_l, c_l), \Sigma_a(r_a, a_a, c_a), \Sigma_t(r_t, a_t, c_t)$, and $\Sigma_\zeta(|\zeta|, a_\zeta, c_\zeta)$ are chosen for the features r_l, r_a, r_t, and ζ, respectively. Sigmoid membership function $\Sigma(r, a, c)$ [see Fig. 12(a)] is described by parameters a, which tunes the slope of the function, and the constant c, which locates the center of the function, respectively,

as follows:

$$\Sigma(r, s, t) = \frac{1}{1 + e^{-a(r-c)}}. \tag{20}$$

Parameters are set as follows:
1) $a_a > 0$;
2) $c_a > 0$;
3) $a_t > 0$;
4) $c_t > 0$;
5) $a_l > 0$;
6) $c_l > 0$;

for the ratio-based features. This indicates a direct proportionality between the ratio value and the probability of a candidate to be a fully destroyed building:
7) $a_\zeta < 0$;
8) $c_\zeta > 0$;

for the orientation feature, indicating an inverse proportionality where the higher the angle (i.e., lower alignment) the lower the probability of a candidate to be a fully destroyed building. For each pair of candidate regions, the aggregate membership $\eta_{\text{FD}} = \Sigma_l \Sigma_a \Sigma_\zeta \Sigma_t$ is computed for a global evaluation. The candidates with η_{FD} greater than a membership threshold $T_\eta^{(\text{FD})}$ are labeled either ω_1 and ω_2, depending on whether R_D appears in near range and R_I in far range or vice versa [22]. The objects detected as ω_1 and ω_2 are masked out from the map M_{opt}, resulting in a map $M_{\text{opt}}^{(\text{mask})}$.

C. Hierarchical Level 2: PDBD

The analysis of the PDBD is structured with the same paradigm of the FDBD, because of the geometrical properties of the multitemporal model for the partially destroyed building (see Section III-B), but it accounts for the different size and spatial properties of the backscattering signature of partial damages. For the second hierarchical level, the changed building candidates are detected from $M_{\text{opt}}^{(\text{mask})}$ by using a sliding window with size parameters z_1 and z_2, scanning from left to right and counting the total number of changed pixels inside the window. The windows keep the same set of orientation values as in Fig. 11. The detection provides a candidate index $C^{(\text{PD})}$ indicating the amount of the change information in the set of windows. A binary map of the candidates $C_{\text{bin}}^{(\text{PD})}$ is derived by thresholding $C^{(\text{PD})}$ with threshold value $T_C^{(\text{PD})}$, chosen based on the size of the moving window (i.e., $T_C^{(\text{PD})} = \tau_{\text{PD}} z_1 z_2, 0 < \tau_{\text{PD}} \leq 1$). The set of candidates is extracted from $C_{\text{bin}}^{(\text{PD})}$ by considering

the connected components, similarly to what done in FDBD. In order to avoid the detection of a large number of small candidates, window size parameters are kept similar to those considered in the first hierarchical level while the threshold value is smaller.

A bounding box is traced for each candidate and a spatial analysis is conducted on region pairs $\tilde{R}_I$ and $\tilde{R}_D$. For the case of building partial destruction, the spatial analysis focuses on the set $\tilde{r}_l, \tilde{r}_a, \tilde{r}_t, \tilde{\zeta}$. For the evaluation, sigmoid membership function $\Sigma_l(\tilde{r}_l, \tilde{a}_l, \tilde{c}_l)$, defined in (20), and Gaussian membership functions $\gamma_a(\tilde{r}_a, \mu_a, \sigma_a), \gamma_t(\tilde{r}_t, \mu_t, \sigma_t)$, and $\gamma_\zeta(\tilde{\zeta}, \mu_\zeta, \sigma_\zeta)$ are chosen according to the physical meaning of features $\tilde{r}_l, \tilde{r}_a, \tilde{r}_t$, and $\tilde{\zeta}$, respectively. Gaussian membership function $\gamma(r, \mu, \sigma)$ [see Fig. 12(b)] is described by parameters μ and σ associated with mean and standard deviation of the function, respectively, as follows:

$$\gamma(r, \mu, \sigma) = e^{\frac{-(r-\mu)^2}{2\sigma^2}}. \tag{21}$$

All the parameters of the four membership functions are set with real positive values. For each pair, the aggregate membership $\eta_{\text{PD}} = \gamma_a \gamma_\zeta \gamma_t \Sigma_l$ is computed. The candidates both presenting a pair of regions with decrease and increase in near and far ranges, respectively, and having a value η_{PD} greater than a membership threshold $T_\eta^{(\text{PD})}$ are classified as building partial destruction (ω_3).

D. CD Map Fusion

An overall building CD map is obtained by combining information from M_{opt} and the output maps from both FDBD and PDBD. Regions of no change in backscattering are labeled as ω_0. Regions of ω_I and ω_D not associated with any of the building models (i.e., $\omega_1, \omega_2, \omega_3$ classes) are labeled as general change (ω_4). Remaining regions of no backscattering variations are labeled as no change (ω_0). The overall building CD map represents $\omega \in \{\omega_0, \omega_1, \omega_2, \omega_3, \omega_4\}$.

V. EXPERIMENTAL RESULTS

In order to validate the proposed approach, two datasets of multitemporal VHR SAR images with size 1024×1024 pixels have been considered. The two datasets describe two residential areas in the city of L'Aquila, Italy, which has been interested by a strong earthquake that caused the collapse of several buildings and relevant damages to many others, together with the death of several civilians. The first dataset is a residential modern area outside the inner city, for which most of the buildings can reasonably be assumed as isolated from the neighbors. The second dataset is near a medieval residential area in the inner city, in which part of the scene presents buildings that are very close to each other and thus single backscattering features of buildings are difficult to be detected at the resolution of the available SAR images. This aspect makes the building CD more complex as building backscattering may slightly differ from the theoretical one because of occlusion from or interaction with neighboring buildings. The selection of the two datasets has been subjected

to both the presence of damaged built-up structures with high severity and the low building density that favors the use of the building scattering model. For both the multitemporal datasets, pre and post-event VHR SAR images have been acquired by the Cosmo-SkyMed constellation in Spotlight mode on April 5th, 2009 and September 12th, 2009, respectively. Both images are in HH polarization, having incidence angle $\theta = 53°$. After standard processing, the level 1C (geocoded ellipsoid corrected) images show a spatial resolution of 1 m and a 0.5 m $\times$ 0.5 m pixel spacing. Radiometric calibration and coregistration were performed.

For the validation, a reference map of the fully and partially destroyed buildings in the area has been derived based on a postevent damage survey conducted on site. The survey provided a building damage map with EMS98 scale [48]. Because of the damage grade and the spatial resolution of the data, the attention was focused on grades 4 (partially destroyed) and 5 (fully destroyed) of the EMS scale. The analysis has been refined to the best of our abilities by a visual inspection of an ortho-photo of the crop acquired after the seismic event and by taking into account the SAR geometry of acquisition. For buildings with lacking information of the EMS damage, the visual inspection has been the only factor for the generation of the reference. Detection accuracy has been evaluated at building level, evaluating the correct detections and misclassifications for the classes ω_1, ω_2, and ω_3. In the following, a more detailed description of the scene and the performance of the proposed approach are reported for the two crops.

A. Crop 1: Modern Residential Area

The first crop has a size of 1024×1024 pixels and represents the southern part of inner city. Fig. 13(a) shows a multitemporal false color composition of the two SAR images of Crop 1, where areas of backscattering increase and decrease appear in magenta and green, respectively. Fig. 13(a) shows the postevent ortho-photo, with red and yellow polygons indicating fully and the partially destroyed buildings, respectively. A total of 200 buildings were counted. Among these, eight buildings were classified as fully destroyed (ω_1), and six as partially destroyed (ω_3).

The proposed approach computed the log-ratio feature X_{LR} and multiscale analysis has been conducted on X_{LR}, generating the sequence $\{X_{\text{LR}}^0, ..., X_{\text{LR}}^{N-1}\}$. The optimal scale level N has been selected considering the average building size and the noise level of the SAR images. It has been demonstrated that the value $N = 4$ preserves radar footprint of buildings with size larger than 8 meters, which is compatible with the minimum size of building footprints in the considered scenario [22]. The impulse response of the filters in the 2D-SWT has been chosen from the Daubechies family with order 4 [43]. The split-based analysis has been conducted on X_{LR}^{N-1} for deriving the backscattering CD map M_{opt}. The split size has been selected by taking into account the average size of the buildings, which was estimated to be $L \times W \times H = 25 \times 20 \times 13 \text{ m}^3$. By following [49], projecting in ground-range geometry and taking into account
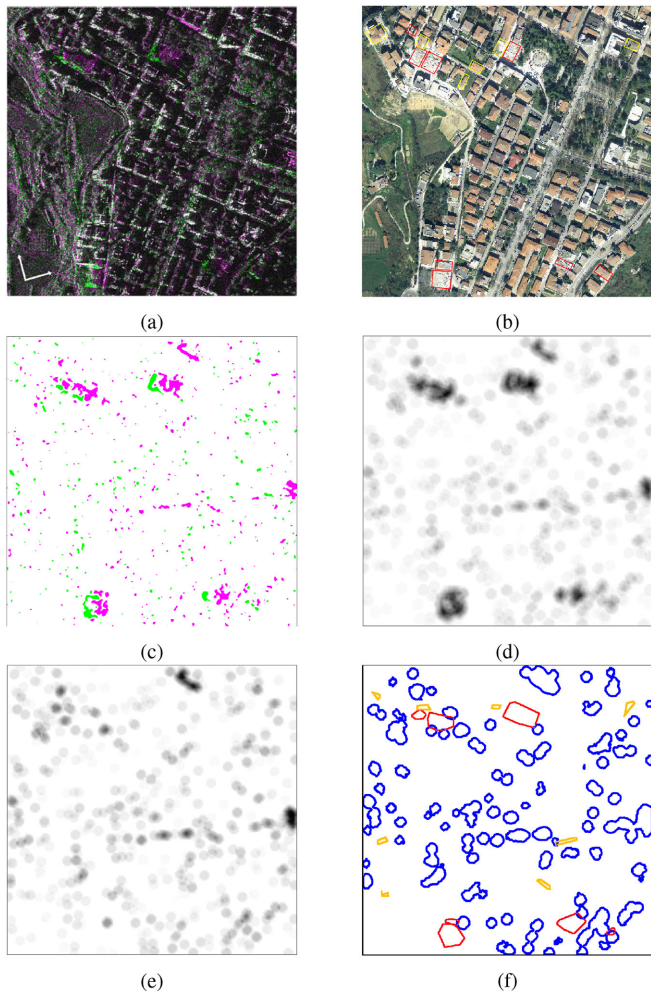
(a)

(b)

(c)

(d)

(e)

(f)

Fig. 13.   Crop 1. (a) Multitemporal false color composition of SAR images (R, B: September 2009, G: April 2009). (b) Optical postevent image. (c) Backscattering CD Map M_{opt}, with increase and decrease represented in magenta and green, respectively. (d) Candidate gray-scale map $C^{(\text{FD})}$. (e) Candidate gray-scale map $C^{(\text{PD})}$. (f) Multiclass building CD map (ω_1 (red), ω_3 (yellow), and ω_4 (blue)).

TABLE IV
PARAMETERS USED IN THE EXPERIMENTS

(a) Common parameters

Parameter	Value
N	4
S_R	120
S_A	40
B	3
z_1	40
z_2	20

(b) FDBD and PDBD specific parameters

FDBD		PDBD	
Parameter	Value	Parameter	Value
τ_{FD}	0.2	τ_{PD}	0.0725
$T_\eta^{(FD)}$	0.125	$T_\eta^{(PD)}$	0.125
a_a	10	μ_a	3.6
c_a	0.3	σ_a	1.55
a_l	10	$\tilde{a}_l$	10
c_l	0.5	$\tilde{c}_l$	0.15
a_ζ	-10	μ_ζ	$\pi/8$
c_ζ	$\pi/3$	σ_ζ	0.4
a_t	30	μ_t	0.45
c_t	0.5	σ_t	0.12

the pixel spacing of 0.5 m along both the range and azimuth directions, it resulted in $S_R = 120$ and $S_A = 40$ pixels. The selection of the splits with highest change content has been conducted by selecting $B = 3$. Previous experimental results conducted on this site [22] (as well as on others [3]) proved how the split-based approach shows robust performance with respect to the change in the split size. In particular, the robustness proved was proved with S_A and S_R ranging in the intervals [20; 60] and [80; 170], respectively [22]. On the samples of the split subset, no-change and change classes have been separated by estimating the statistical unknown parameters with the EM algorithm and applying the Bayesian thresholding. Fig. 13(c) shows the map M_{opt}, in which backscattering increase and decrease are represented in green and magenta, respectively.

FDBD has been conducted on the map, starting with the analysis based on the sliding window for the extraction of the building candidates. FDBD detects the presence of fully destroyed buildings, thus the window size has been selected

comparable to the minimum building footprint, with values $z_1 = 40$ and $z_2 = 20$, respectively [22]. Fig. 13(d) shows the output map generated by the sliding window. Threshold scale value $\tau_{\text{FD}} = 0.2$ (thus $T_C^{(\text{FD})} = 160$) was selected in order to limit the outliers in the candidate analysis. This resulted in a total of 52 building candidates. For each of the building candidates, the proposed fuzzy rules have been applied. Aggregate membership η_{FD} has been derived and thresholded for detecting fully destroyed buildings. The threshold was selected by considering a limit case of 0.6 for the membership function of the single rules, resulting in an aggregate value $T_\eta^{(\text{FD})} = 0.125$ for $\eta_{(\text{FD})}$. The value is compatible with the considerations asserted in [22]. After the masking of the detected buildings on M_{opt}, PDBD has been conducted on the masked map. In order to avoid a large number of small regions, the window size has been selected with same size of that in FDBD. The threshold for the candidates detection in this step has been selected smaller than that required for the FDBD (i.e., $\tau_{\text{PD}} = 0.0725$). The analysis yielded a set of 139 candidates. The proposed fuzzy rules have been applied on the candidates. Aggregate membership η_{PD} has been derived and thresholded. An overview of the parameters considered in the analysis is reported in Table IV. The fuzzy membership function parameters were set according to the physical meaning of the tested features (see Sections III and IV) and in agreement with the results of some initial empirical tests. The method showed to be robust to the selection of these values. The maps obtained with the application of the two fuzzy sets have been fused in the final multiclass building CD map [see Fig. 13(f)].

Table V reports the quantitative assessment for crop 1. With the proposed approach, seven out of eight buildings were correctly labeled as ω_1 (see Fig. 14(a) and [22]), whereas four out of six as ω_3. The three miss detections correspond to fully and partially destroyed buildings labeled as general change and a partially destroyed building labeled as no change, respectively. A

TABLE V
CROP 1: DETECTION ASSESSMENT OF THE PROPOSED APPROACH

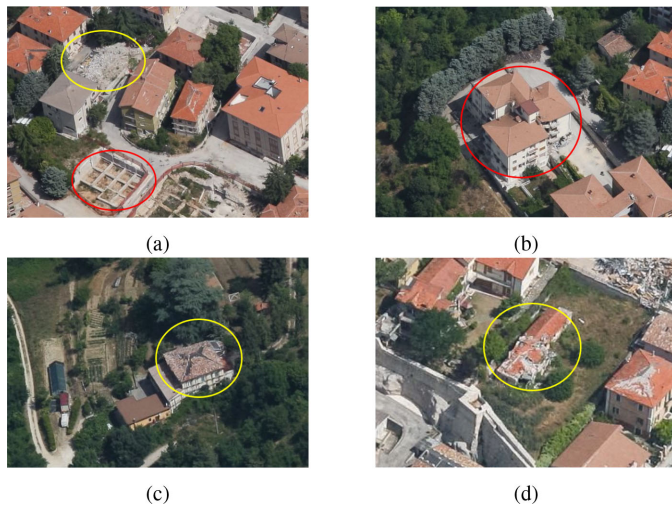| Building Detection Assessment		
Correct Detections		
Fully Destroyed (ω_1)	7	
Partially Destroyed (ω_3)	4	
Missed Detections		
Fully Destroyed	detected as Partially Destroyed (ω_3)	0
	detected as general change (ω_4)	1
	detected as no change (ω_0)	0
Partially Destroyed	detected as Fully Destroyed (ω_1)	0
	detected as general change (ω_4)	1
	detected as no change (ω_0)	1

Fig. 14. Crop 1: Examples for buildings detected by the proposed approach. (a) Miss (above) and correct (below) detections for fully destroyed building class. (b) Correct detection for partially destroyed building class. (c) False alarm for partially destroyed building class. (d) Miss detection for partially destroyed building class.
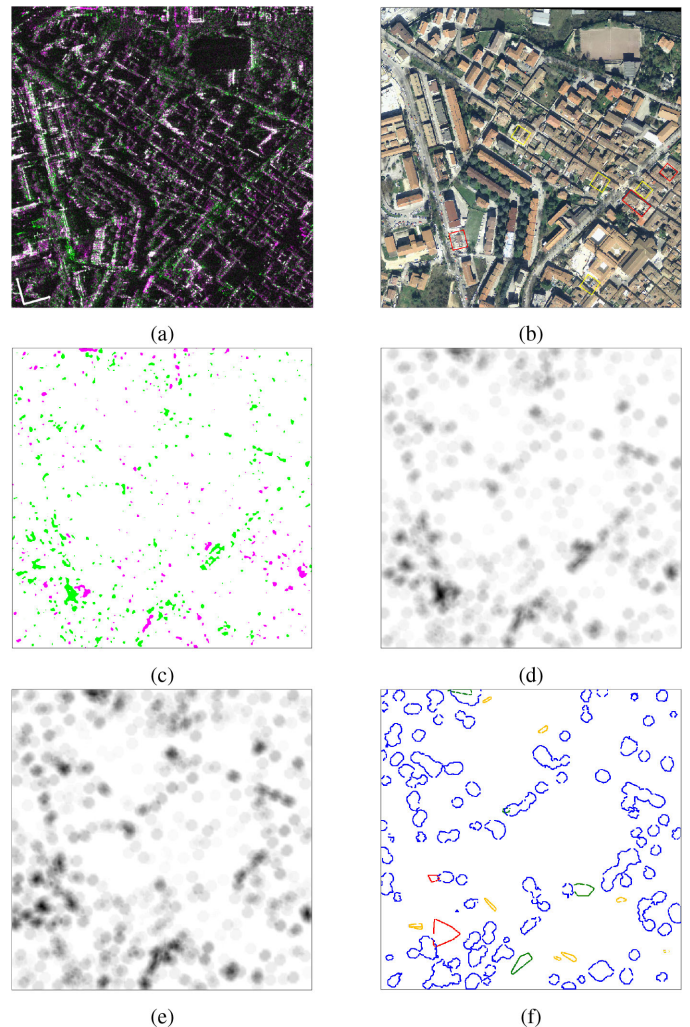

Fig. 15. Crop 2. (a) Multitemporal false color composition of SAR images (R, B: September 2009, G: April 2009). (b) Optical postevent image. (c) Backscattering CD Map M_{opt}, with increase and decrease represented in magenta and green, respectively. (d) Candidate gray-scale map $C^{(FD)}$. (e) Candidate gray-scale map $C^{(PD)}$. (f) Multiclass building CD map (ω_1 (red), ω_2 (green), ω_3 (yellow), and ω_4 (blue)).

total of five false alarms was reported for building misclassified as ω_3. It is worth noting that the five false alarms are buildings not following the model of partially destroyed building, but still characterized by a damage level EMS4 in the survey [48].

From a qualitative analysis, the miss detection of the fully destroyed building (ω_1) may be probably explained by the influence of the surrounding buildings and vegetation on the multitemporal building footprint [see Fig. 14(b) and (c)]. Most of the false alarms can be associated with the presence of vegetated areas close to the buildings, creating a multitemporal behavior for the scattering not clearly predictable nor considerable in the backscattering model [see Fig. 14(d)] [35].

B. Crop 2: Medieval Residential Area

Fig. 15(a) shows the multitemporal false color composition of the two SAR images for the second dataset, with green and magenta mapping the backscattering increase and decrease, respectively. Fig. 15(b) shows the corresponding postevent ortho-photo. From the ortho-photo, 165 buildings were counted. Among these, three were classified as fully destroyed, and four as partially destroyed. The approach considered the generation of the log-ratio X_{LR} and the use of the wavelet-based multiscale

analysis for generating the robust multitemporal feature X_{LR}^{N-1}. $N = 4$ was selected as optimal scale value. Split-based CD analysis was conducted on X_{LR}^{N-1} for generating the backscattering CD map [see Fig. 15(c)]. For the FDBD, a sliding window with size $z_1 = 40$ and $z_2 = 20$ was selected for the candidate detection. Fig 15(d) shows the output map generated by the sliding window in the FDBD. The thresholded map provided a set of 85 possible candidates. The set of fuzzy rules was applied on the building candidates and the aggregate membership η_{FD} was thresholded. An overview of the parameters selected in the fuzzy analysis is presented in Table IV. The fuzzy parameters are selected based on the geometry of the multitemporal signature, the robustness of the fuzzy detection step, and their physical meaning (see Sections III and IV). With the masking of the elements in ω_1 and ω_2, the PDBD analysis was conducted. Same parameters were kept for the sliding window. A threshold scale value $\tau_{PD} = 0.1$ was selected slightly higher in order

TABLE VI
CROP 2: DETECTION ASSESSMENT OF THE PROPOSED APPROACH

Building Detection Assessment		
Correct Detections		
Fully Destroyed	2	
Partially Destroyed	2	
Missed Detections		
Fully Destroyed	detected as Partially Destroyed	1
	detected as general change	0
	detected as no change	0
Partially Destroyed	detected as Fully Destroyed	0
	detected as general change	2
	detected as no change	0

to have a robust detection in the presence of local vegetated areas [see Fig. 15(b)]. This provided a set of 141 candidates. The resulting building candidates have been analyzed with the proposed fuzzy logic set. Thresholding on the aggregate membership values has been finally conducted. The final CD map is reported in Fig. 15(f).

Table VI reports the performance analysis for Crop 2. The proposed approach presents the correct detection of two fully destroyed building (ω_1) and two partially destroyed buildings (ω_3), with the three miss detections, namely one fully destroyed and two partially destroyed buildings. However, it is worth noting that one of the miss detection associated with ω_1 has been detected as ω_3, whereas both the miss detections in ω_3 are labeled as ω_4. In other words, mislabeled partially destroyed buildings do not represent missed alarms since they are detected as changes anyway, this is important in an emergency scenario. The proposed approach introduced six false alarms in the two hierarchical levels, namely one associated with ω_1, two to ω_2, and three for ω_3, respectively. This is a very good result given the complexity of typical Italian Medieval Residential urban scenarios where building density is high with respect to the resolution of the SAR images. Buildings appear juxtaposed or at very small (below the resolution of the sensor) distance and a strong presence of vegetation in the local scene can be observed. In this situation, the backscattering of partially destroyed buildings may slightly differ from the theoretical one because of occlusions from and interaction with the backscattering of neighboring objects. In this perspective, we believe that the method demonstrated very good capabilities in detecting the small changes associated with partially destroyed buildings.

VI. CONCLUSION

In this work, a novel approach for building CD in multitemporal VHR SAR has been presented. The approach defines the building-CD problem as being hierarchical to separate new, fully destroyed, and partially destroyed buildings in light of that they happen at different spatial scales. To this end, a set of fuzzy-based geometrical rules has been defined for each kind of change. The ones associated with partially destroyed buildings are based on the proposed novel single and multitemporal scattering models. The pre- and postevent models are obtained by applying the ray-tracing method and the postevent one makes some assumptions about the geometry and the size of

the building and its damaged part. The multitemporal scattering behavior is computed by comparing the pre and post ones.

Validation has been conducted by considering a pair of VHR SAR images acquired by Cosmo-SkyMed constellation before and after the earthquake in L'Aquila, in 2009. The results highlighted the effectiveness of the approach and the validity of the proposed partially destroyed building model, with the detection of both partially and fully destroyed buildings. It is worth recalling here that the two kinds of change has large relevance in damage assessment and emergency response applications. The approach demonstrated to be accurate on two different kinds of urban structures. As expected, it achieved better performance in the modern regular urban structure than on the more complex and dense historical urban one.

Future developments aim at analyzing the multitemporal signature of buildings with damage interesting other macroelements and integrating their detection in the unsupervised CD strategy. Moreover, we plan to include an *ad hoc* datasets designed for the analysis of performance in detecting new buildings. Furthermore, we will study the detection problem in the presence of dense built-up areas (such as the case of the Italian Medieval Residential dataset), where building footprint is partially affected by surrounding elements.

REFERENCES

[1] B. Chen *et al.*, "Mapping forest and their spatial–temporal changes from 2007 to 2015 in tropical Hainan Island by integrating ALOS/ALOS-2 l-band SAR and Landsat optical images," *IEEE J. Sel. Topics Appl. Earth Observ. Remote Sens.*, vol. 11, no. 3, pp. 852–867, Mar. 2018.

[2] C. Colesanti, A. Ferretti, F. Novali, C. Prati, and F. Rocca, "SAR monitoring of progressive and seasonal ground deformation using the permanent scatterers technique," *IEEE Trans. Geosci. Remote Sens.*, vol. 41, no. 7, pp. 1685–1701, Jul. 2003.

[3] F. Bovolo and L. Bruzzone, "A split-based approach to unsupervised change detection in large-size multitemporal images: Application to Tsunami-damage assessment," *IEEE Tran. Geosci. Remote Sens.*, vol. 45, no. 6, pp. 1658–1670, Jun. 2007.

[4] F. Dell'Acqua, C. Bignami, M. Chini, G. Lisini, D. A. Polli, and S. Stramondo, "Earthquake damages rapid mapping by satellite remote sensing data: L'aquila Apr. 6th, 2009 event," *IEEE J. Sel. Topics Appl. Earth Observ. Remote Sens.*, vol. 4, no. 4, pp. 935–943, Dec. 2011.

[5] P. Gamba, F. Dell'Acqua, and G. Trianni, "Rapid damage detection in the Bam area using multitemporal SAR and exploiting ancillary data," *IEEE Trans. Geosci. Remote Sens.*, vol. 45, no. 6, pp. 1582–1589, Jun. 2007.

[6] Y. Ban and O. A. Yousif, "Multitemporal spaceborne SAR data for urban change detection in China," *IEEE J. Sel. Topics Appl. Earth Observ. Remote Sens.*, vol. 5, no. 4, pp. 1087–1094, Aug. 2012.

[7] L. Giustarini, R. Hostache, P. Matgen, G. J.-P. Schumann, P. D. Bates, and D. C. Mason, "A change detection approach to flood mapping in urban areas using TerraSAR-X," *IEEE Trans. Geosci. Remote Sens.*, vol. 51, no. 4, pp. 2417–2430, Apr. 2013.

[8] P. T. Brett and R. Guida, "Earthquake damage detection in urban areas using curvilinear features," *IEEE Trans. Geosci. Remote Sens.*, vol. 51, no. 9, pp. 4877–4884, Sep. 2013.

[9] H. Maître, *Processing of Synthetic Aperture Radar (SAR) Images*. Hoboken, NJ, USA: Wiley, 2013.

[10] M. Matsuoka and F. Yamazaki, "Use of satellite SAR intensity imagery for detecting building areas damaged due to earthquakes," *Earthquake Spectra*, vol. 20, no. 3, pp. 975–994, 2004.

[11] T. Balz and M. Liao, "Building-damage detection using post-seismic high-resolution SAR satellite data," *Int. J. Remote Sens.*, vol. 31, no. 13, pp. 3369–3391, 2010.

[12] D. Brunner, G. Lemoine, and L. Bruzzone, "Earthquake damage assessment of buildings using VHR optical and SAR imagery," *IEEE Trans. Geosci. Remote Sens.*, vol. 48, no. 5, pp. 2403–2420, May 2010.

[13] R. Guida, A. Iodice, D. Riccio, and U. Stilla, "Model-based interpretation of high-resolution SAR images of buildings," *IEEE J. Sel. Topics Appl. Earth Observ. Remote Sens.*, vol. 1, no. 2, pp. 107–119, Jun. 2008.

[14] S. Karimzadeh and M. Mastuoka, "Building damage assessment using multisensor dual-polarized synthetic aperture radar data for the 2016 M 6.2 Amatrice earthquake, Italy," *Remote Sens.*, vol. 9, no. 4, 2017, Art. no. 330.

[15] S.-W. Chen, X.-S. Wang, and M. Sato, "Urban damage level mapping based on scattering mechanism investigation using fully polarimetric SAR data for the 3.11 East Japan earthquake," *IEEE Trans. Geosci. Remote Sens.*, vol. 54, no. 12, pp. 6919–6929, Dec. 2016.

[16] S.-W. Chen, X.-S. Wang, and S.-P. Xiao, "Urban damage level mapping based on co-polarization coherence pattern using multitemporal polarimetric SAR data," *IEEE J. Sel. Topics Appl. Earth Observ. Remote Sens.*, vol. 11, no. 8, pp. 2657–2667, Aug. 2018.

[17] Y. Bai, B. Adriano, E. Mas, H. Gokon, and S. Koshimura, "Object-based building damage assessment methodology using only post event ALOS-2/PALSAR-2 dual polarimetric SAR intensity images," *J. Disaster Res*, vol. 12, no. 2, pp. 259–271, 2017.

[18] L. Gong, C. Wang, F. Wu, J. Zhang, H. Zhang, and Q. Li, "Earthquake-induced building damage detection with post-event sub-meter VHR TerraSAR-X staring spotlight imagery," *Remote Sens.*, vol. 8, no. 11, 2016, Art. no. 887.

[19] J. Liu, M. Gong, K. Qin, and P. Zhang, "A deep convolutional coupling network for change detection based on heterogeneous optical and radar images," *IEEE Trans. Neural Netw. Learn. Syst.*, vol. 29, no. 3, pp. 545–559, Mar. 2018.

[20] M. Chini, N. Pierdicca, and W. J. Emery, "Exploiting SAR and VHR optical images to quantify damage caused by the 2003 Bam earthquake," *IEEE Trans. Geosci. Remote Sens.*, vol. 47, no. 1, pp. 145–152, Jan. 2009.

[21] L. An, J. Zhang, L. Gong, and Q. Li, "Integration of SAR image and vulnerability data for building damage degree estimation," in *Proc. IEEE Int. Geosci. Remote Sens. Symp., Int.*, 2016, pp. 4263–4266.

[22] C. Marin, F. Bovolo, and L. Bruzzone, "Building change detection in multitemporal very high resolution SAR images," *IEEE Trans. Geosci. Remote Sens.*, vol. 53, no. 5, pp. 2664–2682, May 2015.

[23] F. Baselice, G. Ferraioli, and V. Pascazio, "Markovian change detection of urban areas using very high resolution complex SAR images," *IEEE Geosci. Remote Sens. Lett.*, vol. 11, no. 5, pp. 995–999, May 2014.

[24] P. Uprety, F. Yamazaki, and F. Dell'Acqua, "Damage detection using high-resolution SAR imagery in the 2009 L'aquila, Italy, earthquake," *Earthquake Spectra*, vol. 29, no. 4, pp. 1521–1535, 2013.

[25] J. Inglada and G. Mercier, "A new statistical similarity measure for change detection in multitemporal SAR images and its extension to multiscale change analysis," *IEEE Trans. Geosci. Remote Sens.*, vol. 45, no. 5, pp. 1432–1445, May 2007.

[26] H. Miura, S. Midorikawa, and M. Matsuoka, "Building damage assessment using high-resolution satellite SAR images of the 2010 Haiti earthquake," *Earthquake Spectra*, vol. 32, no. 1, pp. 591–610, 2016.

[27] C. V. Lopez, T. Kempf, R. Speck, H. Anglberger, and U. Stilla, "Automatic change detection using very high-resolution sar images and prior knowledge about the scene," *Proc. SPIE*, vol. 10188, 2017, Art. no. 1018805.

[28] M. Quartulli and M. Datcu, "Stochastic geometrical modeling for built-up area understanding from a single sar intensity image with meter resolution," *IEEE Trans. Geosci. Remote Sens.*, vol. 42, no. 9, pp. 1996–2003, Sep. 2004.

[29] G. Franceschetti, A. Iodice, D. Riccio, and G. Ruello, "SAR raw signal simulation for urban structures," *IEEE Trans. Geosci. Remote Sens.*, vol. 41, no. 9, pp. 1986–1995, Sep. 2003.

[30] S. Auer, S. Hinz, and R. Bamler, "Ray-tracing simulation techniques for understanding high-resolution SAR images," *IEEE Trans. Geosci. Remote Sens.*, vol. 48, no. 3, pp. 1445–1456, Mar. 2010.

[31] A. Ferro, D. Brunner, L. Bruzzone, and G. Lemoine, "On the relationship between double bounce and the orientation of buildings in VHR SAR images," *IEEE Geosci. Remote Sens. Lett.*, vol. 8, no. 4, pp. 612–616, Jul. 2011.

[32] A. R. Brenner and L. Roessing, "Radar imaging of urban areas by means of very high-resolution SAR and interferometric SAR," *IEEE Trans. Geosci. Remote Sens.*, vol. 46, no. 10, pp. 2971–2982, Oct. 2008.

[33] S. Kuny, K. Schulz, and H. Hammer, "Signature analysis of destroyed buildings in simulated high resolution SAR data," in *Proc. IEEE Int. Geosci. Remote Sens. Symp.*, 2013, pp. 903–906.

[34] D. Pirrone, F. Bovolo, and L. Bruzzone, "Analysis of backscattering behaviors for partially damaged buildings in VHR SAR images," in *Proc. SPIE*, vol. 9643, 2015, Paper 96431D.

[35] F. Wu, J. Shan, and C. Wang, "Earthquake-induced collapsed building detection with VHR synthetic aperture radar images," 2017. [Online]. Available: https://docs.lib.purdue.edu/purduegisday/2017/allevents/3/

[36] K. Tang, X. Sun, H. Sun, and H. Wang, "A geometrical-based simulator for target recognition in high-resolution SAR images," *IEEE Geosci. Remote Sens. Lett.*, vol. 9, no. 5, pp. 958–962, Sep. 2012.

[37] J. A. Richards *et al.*, *Remote sensing With Imaging Radar*, vol. 1. New York, NY, USA: Springer, 2009.

[38] D. Wood and C. K. Yap, "The orthogonal convex skull problem," *Discr. Comput. Geometry*, vol. 3, no. 4, pp. 349–365, 1988.

[39] Y. Zheng, X. Zhang, B. Hou, and G. Liu, "Using combined difference image and k-means clustering for SAR image change detection," *IEEE Geosci. Remote Sens. Lett.*, vol. 11, no. 3, pp. 691–695, Mar. 2014.

[40] E. J. Rignot and J. J. Van Zyl, "Change detection techniques for ERS-1 SAR data," *IEEE Trans. Geosci. Remote Sens.*, vol. 31, no. 4, pp. 896–906, Jul. 1993.

[41] H.-C. Li, T. Celik, N. Longbotham, and W. J. Emery, "Gabor feature based unsupervised change detection of multitemporal SAR images based on two-level clustering," *IEEE Geosci. Remote Sens. Lett.*, vol. 12, no. 12, pp. 2458–2462, Dec. 2015.

[42] Y. Bazi, L. Bruzzone, and F. Melgani, "Automatic identification of the number and values of decision thresholds in the log-ratio image for change detection in SAR images," *IEEE Geosci. Remote Sens. Lett.*, vol. 3, no. 3, pp. 349–353, Jul. 2006.

[43] F. Bovolo and L. Bruzzone, "A detail-preserving scale-driven approach to change detection in multitemporal SAR images," *IEEE Trans. Geosci. Remote Sens.*, vol. 43, no. 12, pp. 2963–2972, Dec. 2005.

[44] B. Aiazzi, F. Bovolo, L. Bruzzone, A. Garzelli, D. Pirrone, and C. Zoppetti, "Change detection in multitemporal images through single-and multi-scale approaches," in *Mathematical Models for Remote Sensing Image Processing*. New York, NY, USA: Springer, 2018, pp. 325–355.

[45] B. Aiazzi, L. Alparone, and S. Baronti, "Multiresolution local-statistics speckle filtering based on a ratio Laplacian pyramid," *IEEE Trans. Geosci. Remote Sens.*, vol. 36, no. 5, pp. 1466–1476, Sep. 1998.

[46] C. B. Barber, D. P. Dobkin, and H. Huhdanpaa, "The quickhull algorithm for convex hulls," *ACM Trans. Math. Softw.*, vol. 22, no. 4, pp. 469–483, 1996.

[47] T. J. Ross, *Fuzzy Logic With Engineering Applications*. Hoboken, NJ, USA: Wiley, 2009.

[48] A. Tertulliani, A. Rossi, L. Cucci, and M. Vecchi, "L'aquila (Central Italy) earthquakes: The predecessors of the April 6, 2009 event," *Seismological Res. Lett.*, vol. 80, no. 6, pp. 1008–1013, 2009.

[49] A. J. Bennett and D. Blacknell, "Infrastructure analysis from high resolution SAR and INSAR imagery," in *Proc. IEEE 22nd Digit. Avionics Syst. Conf.*, 2003, pp. 230–235.

Davide Pirrone (Member, IEEE) received the B.Eng. and M.Eng. degrees in electronic enginering from the University of Rome "La Sapienza," Rome, Italy, and the Ph.D. degree in information and communication technologies from the University of Trento, Trento, Italy.

He currently has terminated as a Postdoctoral Fellow from the Université Savoie Mont Blanc, Chambéry, France. He has authored or coauthored several research works in referred conferences, journals, and books. His research interests include digital image processing, synthetic aperture radar (SAR) polarimetry, SAR change detection, remote sensing image analysis, and pattern recognition.

Dr. Pirrone is a Reviewer for various international journals.

Francesca Bovolo (Senior Member, IEEE) received the Laurea (B.S.) and Laurea Specialistica (M.S.) degrees (*summa cum laude*) in telecommunication engineering and the Ph.D. degree in communication and information technologies from the University of Trento, Trento, Italy, in 2001, 2003, and 2006, respectively.

She was a Research Fellow with the University of Trento, until 2013. She is currently the Founder and the Head of Remote Sensing for Digital Earth Unit, Fondazione Bruno Kessler, Trento, Italy, and a member of the Remote Sensing Laboratory, University of Trento, Trento, Italy. She is one of the co-investigators of the Radar for Icy Moon Exploration instrument of the European Space Agency Jupiter Icy Moons Explorer and member of the science study team of the EnVision mission to Venus. Her research interests include remote-sensing image processing, multitemporal remote sensing image analysis, change detection in multispectral, hyperspectral, and synthetic aperture radar images, and very high-resolution images, time-series analysis, content-based time-series retrieval, domain adaptation, and light detection and ranging and radar sounders. She conducts research on these topics within the context of several national and international projects.

Dr. Bovolo is a member of the program and scientific committee of several international conferences and workshops. She has been an Associate Editor for the IEEE JOURNAL OF SELECTED TOPICS IN APPLIED EARTH OBSERVATIONS AND REMOTE SENSING, since 2011 and a Guest Editor of the Special Issue on Analysis of Multitemporal Remote Sensing Data of the IEEE TRANSACTIONS ON GEOSCIENCE AND REMOTE SENSING. She is a Referee for several international journals. She was a recipient of the First Place in the Student Prize Paper Competition of the 2006 IEEE International Geoscience and Remote Sensing Symposium (Denver, 2006). She was the Technical Chair of the Sixth and Eight International Workshops on the Analysis of Multitemporal Remote-Sensing Images (MultiTemp 2011 and 2019). She has been a Co-Chair for the SPIE International Conference on Signal and Image Processing for Remote Sensing, since 2014. She was the Publication Chair of the International Geoscience and Remote Sensing Symposium, in 2015.

Lorenzo Bruzzone (Fellow, IEEE) received the Laurea (M.S.) degree in electronic engineering (*summa cum laude*) and the Ph.D. degree in telecommunications from the University of Genoa, Genoa, Italy, in 1993 and 1998, respectively.

He is currently a Full Professor of Telecommunications with the University of Trento, Trento, Italy, where he teaches remote sensing, radar, and digital communications. He is the founder and the director of the Remote Sensing Laboratory with the Department of Information Engineering and Computer Science, University of Trento. He is the author or coauthor of 276 scientific publications in referred international journals (209 in IEEE journals), more than 330 papers in conference proceedings, and 22 book chapters. He is an Editor/Coeditor of 18 books/conference proceedings and 1 scientific book. His current research interests are in the areas of remote sensing, radar and synthetic aperture radar, signal processing, machine learning, and pattern recognition. He promotes and supervises research on these topics within the frameworks of many national and international projects. He is the Principal Investigator of many research projects. Among the others, he is currently the Principal Investigator of the Radar for Icy Moon Exploration instrument in the framework of the Jupiter Icy Moons Explorer mission of the European Space Agency (ESA), and the Science Lead for the High Resolution Land Cover project in the framework of the Climate Change Initiative of ESA.

Dr. Bruzzone is currently an Associate Editor for the IEEE TRANSACTIONS ON GEOSCIENCE AND REMOTE SENSING. He was a Guest Co-Editor of many special issues of international journals. He is the cofounder of the IEEE International Workshop on the Analysis of Multi-Temporal Remote-Sensing Images series and is currently a member of the Permanent Steering Committee of this series of workshops. Since 2003, he has been the Chair of the SPIE Conference on Image and Signal Processing for Remote Sensing. He was the founder of the *IEEE Geoscience and Remote Sensing Magazine* for which he has been Editor-in-Chief in between 2013 and 2017. He has been Distinguished Speaker of the IEEE Geoscience and Remote Sensing Society between 2012 and 2016. His papers are highly cited, as proven from the total number of citations (more than 34 000) and the value of the h-index (87) (source: Google Scholar). He was invited as a keynote speaker in more than 40 international conferences and workshops. Since 2009, he has been a member of the Administrative Committee of the IEEE Geoscience and Remote Sensing Society, where since 2019, he has been the Vice-President for Professional Activities. He ranked first place in the Student Prize Paper Competition of the 1998 IEEE International Geoscience and Remote Sensing Symposium (IGARSS), Seattle, July 1998. He was the recipient of many international and national honors and awards, including the recent IEEE GRSS 2015 Outstanding Service Award, the 2017 and 2018 IEEE IGARSS symposium prize paper awards, and the 2019 WHISPER Outstanding Paper Award.